SWIFT PANCHROMATIC OBSERVATIONS OF THE BRIGHT GAMMA-RAY BURST GRB 050525a

A. J. Blustin,[1] D. Band,[2] S. Barthelmy,[2] P. Boyd,[2] M. Capalbi,[3] S. T. Holland,[2] F. E. Marshall,[2] K. O. Mason,[1] M. Perri,[3]
T. Poole,[1] P. Roming,[4] S. Rosen,[1] P. Schady,[1,4] M. Still,[2] B. Zhang,[5] L. Angelini,[2] L. Barbier,[2] A. Beardmore,[6]
A. Breeveld,[1] D. N. Burrows,[4] J. R. Cummings,[2] J. Canizzo,[2] S. Campana,[7] M. M. Chester,[4] G. Chincarini,[7]
L. R. Cominsky,[8] A. Cucchiara,[4] M. de Pasquale,[1] E. E. Fenimore,[9] N. Gehrels,[2] P. Giommi,[3] M. Goad,[6]
C. Gronwall,[4] D. Grupe,[4] J. E. Hill,[2] D. Hinshaw,[2] S. Hunsberger,[4] K. C. Hurley,[10] M. Ivanushkina,[4]
J. A. Kennea,[4] H. A. Krimm,[2] P. Kumar,[11] W. Landsman,[2] V. La Parola,[12] C. B. Markwardt,[2]
K. McGowan,[1] P. Mészáros,[4] T. Mineo,[12] A. Moretti,[7] A. Morgan,[4] J. Nousek,[4]
P. T. O'Brien,[6] J. P. Osborne,[6] K. Page,[6] M. J. Page,[1] D. M. Palmer,[9]
A. M. Parsons,[2] J. Rhoads,[13] P. Romano,[7] T. Sakamoto,[2] G. Sato,[14]
G. Tagliaferri,[7] J. Tueller,[2] A. A. Wells,[6] and N. E. White[2]

ABSTRACT

The bright gamma-ray burst GRB 050525a has been detected with the *Swift* observatory, providing unique multi-wavelength coverage from the very earliest phases of the burst. The X-ray and optical/UV afterglow decay light curves both exhibit a steeper slope ∼0.15 days after the burst, indicative of a jet break. This jet break time combined with the total gamma-ray energy of the burst constrains the opening angle of the jet to be $3°2$. We derive an empirical "time-lag" redshift from the BAT data of $\hat{z} = 0.69 \pm 0.02$, in good agreement with the spectroscopic redshift of 0.61. Prior to the jet break, the X-ray data can be modeled by a simple power law with index $\alpha = -1.2$. However, after 300 s the X-ray flux brightens by about 30% compared to the power-law fit. The optical/UV data have a more complex decay, with evidence of a rapidly falling reverse shock component that dominates in the first minute or so, giving way to a flatter forward shock component at later times. The multiwavelength X-ray/UV/optical spectrum of the afterglow shows evidence for migration of the electron cooling frequency through the optical range within 25,000 s. The measured temporal decay and spectral indexes in the X-ray and optical/UV regimes compare favorably with the standard fireball model for gamma-ray bursts assuming expansion into a constant-density interstellar medium.

Subject headings: astrometry — galaxies: distances and redshifts — gamma rays: bursts — shock waves — X-rays: individual (GRB 050525a)

Online material: color figures

1. INTRODUCTION

The observation of gamma-ray bursts (GRBs) has entered a new era with the launch of the *Swift* observatory (Gehrels et al. 2004). *Swift* provides rapid notification of GRB triggers to the ground using its sensitive Burst Alert Telescope (BAT; Barthelmy et al. 2006) and can make panchromatic observations of the burst and its afterglow by bringing its narrow-field X-Ray Telescope (XRT; Burrows et al. 2006) and UltraViolet/Optical Telescope (UVOT; Roming et al. 2006a) to bear within about 1 minute of the burst going off.

In this paper we describe *Swift* observations of GRB 050525a, the first bright, low-redshift burst to have been observed with *Swift* with both its narrow-field instruments. This has resulted in the most complete multiwavelength description of the early evolution of a burst afterglow yet obtained. We describe the light curve decay in the X-ray and optical/UV bands and compare these with the predictions of theoretical models. We also consider how the multiwavelength spectrum of the burst afterglow evolves with time, making use of the simultaneous X-ray/UV/optical coverage. We combine the measurements of the afterglow properties with the well-constrained measurements of the prompt gamma-ray emission to constrain the geometry of the burst emission. We present an analysis of the prompt gamma-ray emission in § 2.1. This is followed by an analysis of the time evolution and spectrum of the X-ray data in § 2.2, to which we add the optical and ultraviolet data in § 2.3 to build up the multiwavelength picture. The results are discussed in § 3.

2. OBSERVATIONS AND ANALYSIS

2.1. *BAT*

At 00:02:53.26 UT on 2005 May 25, the *Swift* Burst Alert Telescope triggered and located on board GRB 050525a (trigger 130,088). The BAT location calculated on board was R.A. = $278°144$, decl. = $+26°340$ (J2000.0) with an uncertainty of 4′

[1] Department of Space and Climate Physics, Mullard Space Science Laboratory, University College London, Holmbury St. Mary, Dorking, Surrey, RH5 6NT, UK; ajb@mssl.ucl.ac.uk.

[2] NASA Goddard Space Flight Center, Greenbelt, MD 20771.

[3] ASI Science Data Center, via Galileo Galilei, I-00044 Frascati (Rome), Italy.

[4] Department of Astronomy and Astrophysics, Pennsylvania State University, 525 Davey Laboratory, University Park, PA 16802.

[5] Department of Physics, University of Nevada at Las Vegas, 4505 South Maryland Parkway, Las Vegas, NV 89154.

[6] Department of Physics and Astronomy, University of Leicester, University Road, Leicester LE1 7RH, UK.

[7] INAF–Osservatorio Astronomico di Brera, via Bianchi 46, I-23807 Merate, Italy.

[8] Department of Physics and Astronomy, Sonoma State University, 1801 East Cotati Avenue, Rohnert Park, CA 94928.

[9] Los Alamos National Laboratory, P.O. Box 1663, Los Alamos, NM 87545.

[10] Space Sciences Laboratory, University of California at Berkeley, 7 Gauss Way, Berkeley, CA 94720.

[11] Department of Astronomy, University of Texas, RLM 15.308, Austin, TX 78712-1083.

[12] INAF–Istituto di Astrofisica Spaziale e Cosmica, via Ugo La Malfa 153, I-90146 Palermo, Italy.

[13] Space Telescope Science Institute, 3700 San Martin Drive, Baltimore, MD 21218.

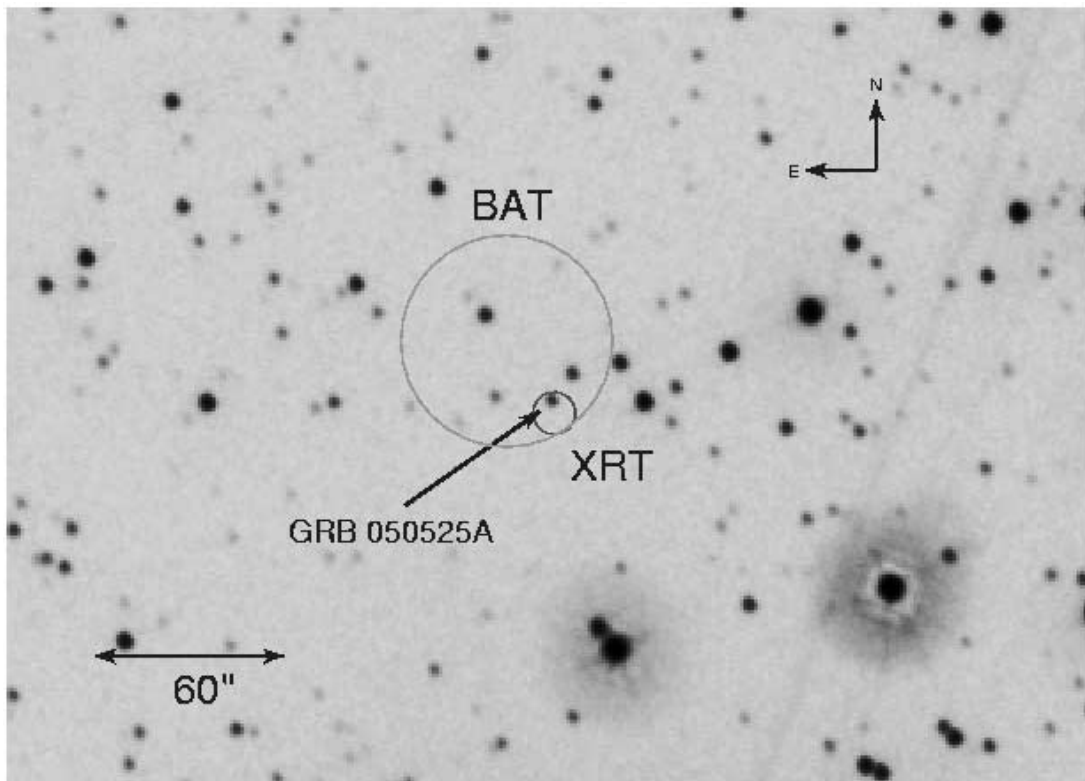[14] Institute of Space and Astronautical Science, Kanagawa 229-8510, Japan.

Fig. 1.—Plot of the field containing GRB 050525a, marking the location of the optical afterglow (the object picked out by the arrow). The BAT error circle is based on the refined ground-based analysis (Cummings et al. 2005), and this has a radius of 0′.5. The XRT error circle has a radius of 6″, and the central position has been revised compared to that reported in Band et al. (2005) after ground analysis. [*See the electronic edition of the Journal for a color version of this figure.*]

(radius 3 σ, including estimated systematic uncertainty). This was later refined (see Fig. 1) to R.A. $= 278°.140$, decl. $= +26°.344 \pm 0′.5$ (95% containment, the position corresponding to R.A. $= 18^h32^m34^s$, decl. $= +26°20′38″$) using the full data set downloaded through the Malindi groundstation ~ 1 hr after the burst. The refined position is $26″$ from the on-board location and $21″$ from the UVOT location. The burst was $28°$ off the BAT bore sight (85% coded) and was 148σ in the image-domain full data set. The spacecraft completed the automated slew to the burst at 00:04:58 UT (75 s after the trigger), and XRT and UVOT began their standard follow-up observation sequences.

Figure 2 shows the BAT light curves in the four standard BAT energy bands. The burst was very bright and was detected in all four energy bands, with a peak rate of $\sim 80,000$ counts s^{-1}. The burst has two main peaks with several smaller peaks within the main structure. The lag between the light curves in the 100–350 and the 25–50 keV bands is $\tau = 0.124 \pm 0.006$ s (the high-energy band leads the low-energy band). The total duration was ~ 12 s (T_{90} is 8.8 ± 0.5 s). The successful trigger criterion for this burst was in the 25–100 keV band with a duration of 64 ms.

Another very bright burst occurred ~ 2800 s later (GRB 050525b; Golenetskii et al. 2005). This was outside the field of view (FOV) of *INTEGRAL*'s IBIS instrument, whereas GRB 050525a was inside the IBIS FOV. Thus, we can be confident that this second burst was not associated with GRB 050525a (Mereghetti et al. 2005).

We fit the BAT spectra using the current analysis techniques developed by the instrument team. Systematic effects are still being resolved this early in the mission, and consequently the fits described here should be regarded as preliminary. To reproduce the known spectrum of the Crab, empirical correction factors have been applied to the prelaunch response matrix; this analysis also
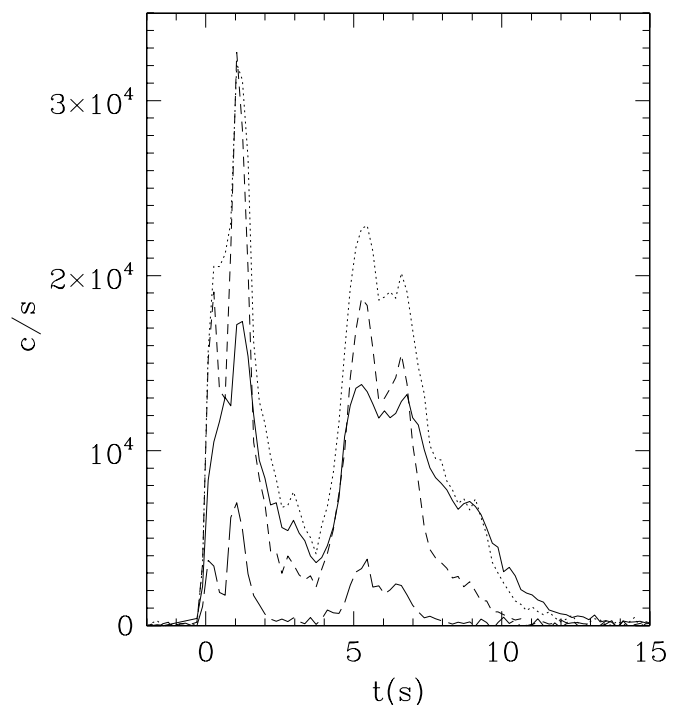

Fig. 2.—BAT light curve of GRB 050525a in the 15–25 keV (*solid line*), 25–50 keV (*dotted line*), 50–100 keV (*short-dashed line*), and 100–350 keV (*long-dashed line*) bands.

TABLE 1
BAT Spectral Fits

Parameter	Entire Burst			Peak Flux		
	Power Law[a]	Power Law, Cutoff[b]	Band Model[c]	Power Law[a]	Power Law, Cutoff[b]	Band Model[c]
β[d]	-0.78[e]	$0.01^{+0.11}_{-0.12}$	$0.01^{+0.11}_{-0.12}$	-0.42[e]	$0.45^{+0.14}_{-0.14}$	$-0.45^{+0.14}_{-0.14}$
β_2[f]	...	...	$-7.84^{+6.40}_{-1.16}$	...	...	$-8.27^{+7.14}_{-0.73}$
E_p[g]	...	$78.8^{+3.9}_{-3.1}$	$78.8^{+3.7}_{-3.1}$	...	$102.4^{+7.1}_{-6.3}$	$102.4^{+8.1}_{-6.3}$
Norm	7.15[e, h]	$14.2^{+5.9i}_{-4.2}$	$15.0^{+1.65h}_{-1.45}$	19.35[e, h]	$7.62^{+3.91i}_{-2.65}$	$44.00^{+6.05h}_{-5.20}$
$\chi^2/$dof	181.7/57	15.2/56	15.2/55	169.8/57	31.6/56	31.6/55

[a] Power-law model: $F(E) \propto E^{\beta}$.
[b] Power law with an exponential cutoff: $F(E) \propto E^{\beta} \exp(-E/E_0)$.
[c] Band model (Band et al. 1993): a low-energy power law with an exponential cutoff transitioning to a high-energy power law, $F(E) \propto E^{\beta_2}$.
[d] The low-energy spectral index.
[e] Fit too poor to produce uncertainty range.
[f] The high-energy spectral index. The fit is insensitive to $\beta_2 < -2.5$ for the fitted value of E_p.
[g] The energy of the peak of $EN(E) \propto \nu f_\nu$, and $E_p = (2 + \beta)E_0$.
[h] The normalization of the spectrum at 50 keV, in units of keV cm^{-2} s^{-1} keV^{-1}.
[i] The normalization of the spectrum at 1 keV, in units of keV cm^{-2} s^{-1} keV^{-1}.

resulted in an estimate of the energy-dependent systematic error that should be added to the statistical error. The corrections and the systematic error are posted online.[15] The count spectra are binned between 16 and 148.8 keV in ~2 keV bins. Table 1 summarizes the spectral fits to the entire burst (12.80 s) and to the peak 1 s, with 90% confidence limits. We fit the count spectra with three nested models, here presented as energy spectra:[16] a power law, $F(E) \propto E^{\beta}$; a power law with an exponential cutoff, $F(E) \propto E^{\beta} \exp(-E/E_0)$; and the Band model (Band et al. 1993), a low-energy power law with an exponential cutoff that transitions into a high-energy power law, $F(E) \propto E^{\beta_2}$. The peak energy $E_p = (1 + \beta)E_0$ is both physically more relevant and less correlated with β than E_0; here E_p is the energy of the peak of $EF(E) \propto \nu f_\nu$. The power law with an exponential cutoff is the same as the Band model with $\beta_2 = -\infty$, and the power-law model is the same as the other two models with $E_0 = \infty$.

As can be seen from these fits, the power-law fit is definitely inferior to the other two spectral models, and the second and third spectral models are equivalent in this case, since the transition to the high-energy power law at $E_b = (\beta - \beta_2)E_0 = (\beta - \beta_2)E_p/(\beta + 1)$ is above 150 keV (the energy of the highest pulse-height analyzer [PHA] channel that is fitted); indeed, for the observed β and E_p values, the fits are insensitive to $\beta_2 < -2.5$.

Konus-*Wind* (Golenetskii et al. 2005) and *INTEGRAL* (Gotz et al. 2005) both detected GRB 050525a. Golenetskii et al. (2005) fit the Konus-*Wind* spectrum from 20 keV to 1 MeV for the entire burst with a power law with an exponential cutoff model and find $\beta = -0.10 \pm 0.05$ and $E_p = 84.1 \pm 1.7$ keV, consistent with the *Swift* fit.

The spectral fits can be integrated over energy and time to give a fluence $S(15-350$ keV$) = (2.01 \pm 0.05) \times 10^{-5}$ ergs cm^{-2} and a peak flux of $P(15-350$ keV$) = 47.7 \pm 1.2$ photons cm^{-2} s^{-1}. Using the observed redshift of $z = 0.606$ (Foley et al. 2005), the spectral fits, and a standard cosmology ($\Omega_m = 0.3$, $\Omega_\Lambda = 0.7$, and $H_0 = 70$ km s^{-1} Mpc^{-1}), we find $E_{\rm iso} = 2.3 \times 10^{52}$ ergs and $L_{\rm iso} = 7.8 \times 10^{51}$ ergs s^{-1}. These two derived quantities are the total energy and peak luminosity that would have been radiated if the observed flux were emitted isotropically. As will be dis-

cussed below (§ 3) in considering the possible jet break, the emission was most likely beamed and the actual emitted energy and luminosity were consequently smaller. Using the redshift, the peak energies in the burst frame are $E_{\rm pp} = 164.5 \pm 11.6$ keV for the peak of the light curve and $E_{\rm pt} = 126.6 \pm 5.5$ keV for the entire burst.

2.2. XRT Data

The XRT observations started on 2005 May 25 at 00:04:08 UT, 75 s after the trigger. The XRT was undergoing engineering tests at the time of the burst, and the Auto state (which selects the observing mode on the basis of source brightness) was disabled. A sequence of three frames in photon-counting (PC) mode were taken first, between $T + 75$ s and $T + 83$ s. These early PC mode data suffer from severe pileup because of the brightness of the source and have been excluded from the analysis.

Shortly afterward, the instrument was put into Auto state, and a 2.5 s exposure in image mode was taken starting at 00:04:58 UT, 125 s after the BAT burst trigger. A bright X-ray source was found near the center of the field of view. The refined X-ray coordinates are R.A. = $18^h32^m32\overset{s}{.}6$ and decl. = $26°20'18''$ (J2000.0), with an estimated positional uncertainty of $6''$ (90% confidence level). The XRT coordinates are $4''$ from the UVOT position of the optical counterpart (see below).

Following the automatic sequence of readout modes, designed to avoid any pileup effect, the instrument was configured in the photodiode (PD) readout mode starting from 00:05:01 UT ($T + 128$ s). Due to the engineering tests mentioned above, the instrument remained in PD mode until 00:20:21 UT ($T + 1048$ s) even when the afterglow brightness was below the nominal flux threshold used for this mode.

Data in PC mode, the most sensitive XRT operational mode, were taken starting at 01:40:32 UT ($T + 5859$ s) until 11:39:11 UT ($T + 41,778$ s). The GRB 050525a field was reobserved in PC mode on several occasions up to late June in 2005.

2.2.1. Temporal Analysis

For the PD mode, events for the temporal analysis were selected in the 0.4–4.5 keV energy band to avoid contamination from the calibration sources. The standard grade selection for this mode (0–5) was used. The count rate was converted to unabsorbed 2–10 keV flux using the best-fit spectral model (see below).

---

[15] Available at http://legacy.gsfc.nasa.gov/docs/swift/analysis/bat_digest.html.

[16] We use the notation β here and throughout the paper to denote the power-law index of the energy spectrum of the source.
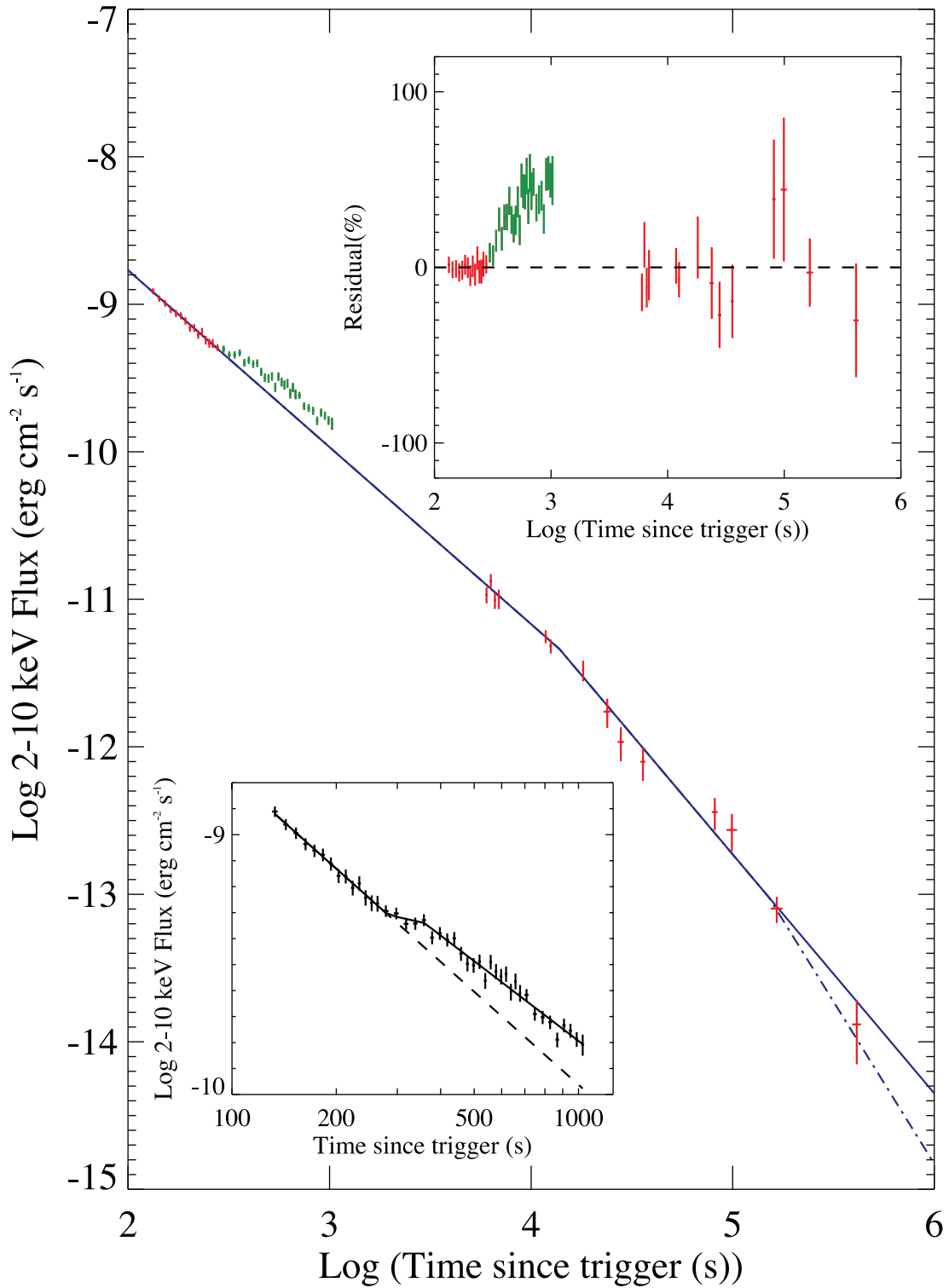
FIG. 3.—XRT decay light curve of GRB 050525a, including both photodiode mode ($T < 2000$ s) and photon-counting mode ($T > 2000$ s) data. The solid line shows a broken power-law fit to the combined data, excluding those photodiode mode points colored green (see text). The dash-dotted line is shown for illustration and has a slope of $\alpha = -2.2$, which is the value expected from simple modeling of a jet break (see text). The lower inset shows the data taken in photodiode mode only, during the first ~ 1000 s after the BAT trigger. The solid line shows a fit to the data with a power-law model that includes two temporal breaks to different decay rates. The dashed line gives an extrapolation of a simple power-law fit (single slope) to the first segment of data prior to about 300 s. The upper inset shows the residuals with respect to the two power-law model fit to all the data, expressed as a percentage of the predicted model flux.

For PC data, events were selected in the 0.3–10 keV band, and grades 0–12 were used in the analysis. Furthermore, since two-dimensional spatial information is available for this mode, photons within a circle of 10 pixel (~24″) radius, which encloses about 80% of the point-spread function at 1.5 keV, were extracted, centered on the source position. The background was estimated from a nearby source-free circular region with 50 pixel radius. Again, the count rate in the 0.3–10 keV band was converted to unabsorbed 2–10 keV flux using the best-fit spectral model.

The background-subtracted 2–10 keV light curve in the time interval from $T + 128$ s to $T + 1048$ s (PD mode) is shown in Figure 3 (*bottom inset*). The X-ray afterglow of GRB 050525a is clearly fading. The early afterglow decay was first fitted with a single power-law model, resulting in a best-fit decay index of $\alpha = -0.95 \pm 0.03$, with $\chi_r^2 = 1.17$ (42 degrees of freedom [dof]). Inspection of the residuals to the best-fit model suggests that a flattening of the decay curve or a rebrightening of the source occurs at ~300 s after the trigger. A better fit is provided by a broken power-law model with slopes α_1 and α_2 and a break at t_b. This model gave $\chi_r^2 = 0.98$ (40 dof), with best-fit parameters $\alpha_1 = -1.23^{+0.03}_{-0.02}$, $\alpha_2 = -0.91$, and $t_b = 203$ s.

Again, however, the residuals suggest systematic deviations from this model. We thus tried a broken power law with two temporal breaks. This model provided a very good fit to the data, with $\chi_r^2 = 0.72$ (38 dof), and is plotted in Figure 3 (*bottom inset*) as a solid line. The best-fit parameters are $\alpha_1 = -1.19$, $t_b^1 = 282$ s, $\alpha_2 = -0.30$, $t_b^2 = 359$ s, and $\alpha_3 = -1.02$.

Next we fitted the X-ray data taken in PC mode at times more than 5000 s after the trigger. We first used a single power-law model, obtaining a best-fit decay index $\alpha = -1.51 \pm 0.07$, with $\chi_r^2 = 1.40$ (12 dof). The poor fit is the result of a clear steepening of the light curve with time. We thus tried a broken power-law model. The model provided a very good fit, with $\chi_r^2 = 0.97$ (10 dof) and best-fit parameters $\alpha_1 = -1.16$, $\alpha_2 = -1.62$, and $t_b = 13{,}177$ s.

Finally, we tried fitting the total light curve derived from the combined PD and PC mode data (see Fig. 3). We find that the power-law fit to the prebrightening PD mode data ($T < 280$ s) extrapolates well to the prebreak PC mode data. Moreover, the decay index before 280 s agrees well with that of the PC mode data before the 13 ks break. In contrast, if we extrapolate the postbrightening PD mode data to later times using the best-fit slope, a significant excess is predicted compared with the measured PC mode data. To join the postbrightening PD mode data to the PC mode data requires a model with at least two temporal breaks, which are not constrained because of the intervening gap in X-ray coverage. We conclude that the brightening at about 280 s in the PD mode data represents a flare in the X-ray flux, possibly similar to the sometimes much larger flares that are seen at early times in other bursts (Burrows et al. 2005; Piro et al. 2005), and that the flux returns to the preflare decay curve prior to the start of our PC mode data.

We thus fit the combined PD and PC mode data, excluding PD data at times $t > T + 288$ s (Fig. 3, *green points*). A broken power-law model provided a good fit (Fig. 3, *solid line*), with $\chi_r^2 = 0.50$ (25 dof) and best-fit parameters $\alpha_1 = -1.20 \pm 0.03$, $\alpha_2 = -1.62^{+0.11}_{-0.16}$, and $t_b = 13{,}726^{+7469}_{-5123}$ s. The break time is thus ~3.8 hr. The complete XRT data are recorded in Table 2.

2.2.2. *Spectral Analysis*

The photodiode spectra in the time intervals from $T + 128$ s to $T + 288$ s ("preflare") and from $T + 288$ s to $T + 1048$ s ("flare") have been extracted in the 0.4–4.5 keV band. The spectra were

TABLE 2
XRT 2–10 keV Flux

T(mid)[a] (s)	T(exp) (s)	Flux[b]
133	5.0	122.7 ± 5.7
143	5.0	109.5 ± 5.4
153	5.0	101.4 ± 5.2
163	5.0	92.0 ± 4.9
173	5.0	86.8 ± 4.8
183	5.0	83.7 ± 4.7
193	5.0	77.2 ± 4.5
203	5.0	69.4 ± 4.3
213	5.0	69.2 ± 4.3
223	5.0	62.4 ± 4.1
233	5.0	65.0 ± 4.1
243	5.0	57.2 ± 3.9
253	5.0	54.6 ± 3.8
263	5.0	54.3 ± 3.8
278	10.0	50.8 ± 2.6
298	10.0	49.8 ± 2.6
318	10.0	45.4 ± 2.5
338	10.0	45.5 ± 2.5
358	10.0	46.9 ± 2.5
378	10.0	40.2 ± 2.3
398	10.0	41.7 ± 2.4
418	10.0	39.4 ± 2.3
438	10.0	39.9 ± 2.3
458	10.0	34.8 ± 2.2
478	10.0	31.9 ± 2.1
498	10.0	31.5 ± 2.1
518	10.0	32.5 ± 2.1
538	10.0	27.4 ± 1.9
558	10.0	32.4 ± 2.1
578	10.0	29.8 ± 2.0
598	10.0	28.5 ± 2.0
618	10.0	29.1 ± 2.0
638	10.0	24.8 ± 1.8
658	10.0	27.3 ± 1.9
678	10.0	24.6 ± 1.8
708	20.0	24.2 ± 1.3
748	20.0	20.4 ± 1.2
788	20.0	19.8 ± 1.2
828	20.0	19.0 ± 1.1
868	20.0	16.3 ± 1.1
908	20.0	18.5 ± 1.1
948	20.0	17.6 ± 1.1
988	20.0	16.3 ± 1.1
1028	20.0	15.5 ± 1.4
6009	150.0	1.072 ± 0.134
6309	150.0	1.331 ± 0.153
6609	150.0	0.987 ± 0.126
6909	150.0	1.010 ± 0.152
11809	350.0	0.560 ± 0.056
12509	350.0	0.482 ± 0.052
18109	350.0	0.331 ± 0.052
23859	2000.0	0.173 ± 0.039
27859	2000.0	0.108 ± 0.028
35859	2000.0	0.079 ± 0.021
81459	5400.0	0.0361 ± 0.0088
99102	11850.0	0.0273 ± 0.0078
165485	22000.0	0.0080 ± 0.0016
412515	42000.0	0.0013 ± 0.0006

[a] Time since trigger.
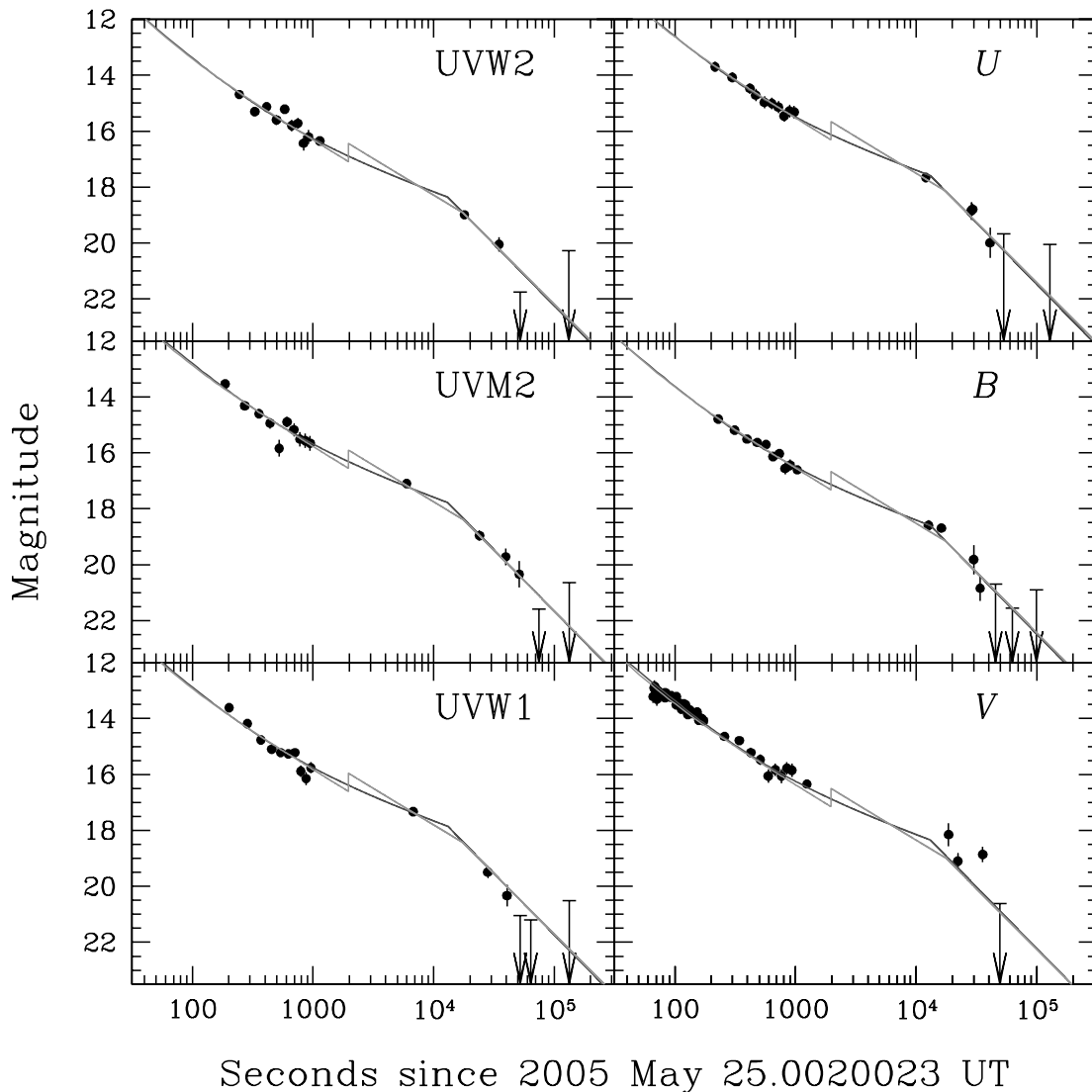[b] Flux in units of 10^{-11} ergs cm^{-2} s^{-1} (2–10 keV).

Fig. 4.—Photometry (*filled circles*) in the six UVOT broadband filters. Arrows indicate 3 σ upper limits to the photometry. A model light curve (*dark gray line*) with $\alpha_1 = -1.56$, $\alpha_2 = -0.62$, $\alpha_j = -1.76$, $t_t = 432$ s (7.2 minutes), and $t_j = 13{,}133$ s (0.152 days) is shown. The light gray line indicates a rebrightening model with $\alpha_1 = -2.14$, $\alpha_2 = -1.04$, $\alpha_j = -1.73$, $t_t = 39$ s, and $t_j = 17{,}747$ s (0.205 days). The flux has been normalized for each filter. [*See the electronic edition of the Journal for a color version of this figure.*]

binned to ensure a minimum of 20 counts bin^{-1} and were fitted using the XSPEC package (ver. 11.3.2; Arnaud 1996).

An absorbed power-law model fits both spectra well. For the preflare spectrum the best-fit hydrogen-equivalent column density is $N_H = (2.00 \pm 0.25) \times 10^{21}$ cm^{-2}, and the energy index is $\beta = -0.99 \pm 0.09$ ($\chi_r^2 = 0.94$; 176 dof). The best-fit parameters for the flare spectrum are $N_H = (2.07 \pm 0.18) \times 10^{21}$ cm^{-2} and $\beta = -0.96 \pm 0.07$ ($\chi_r^2 = 1.04$; 238 dof).

Freezing N_H to the Galactic value (9.0×10^{20} cm^{-2}) and adding a hydrogen-equivalent column density at the redshift of the GRB ($z = 0.606$), we found $N_H^z = (2.2 \pm 0.5) \times 10^{21}$ cm^{-2} and $\beta = -0.90 \pm 0.08$ ($\chi_r^2 = 0.96$; 176 dof) for the preflare spectrum and $N_H^z = (2.5 \pm 0.4) \times 10^{21}$ cm^{-2} and $\beta = -0.89 \pm 0.06$ ($\chi_r^2 = 1.01$; 238 dof) for the flare spectrum.

Events in PC mode from the time interval from $T + 5859$ s to $T + 41{,}778$ s were extracted from the same circular region used in the temporal analysis. A further selection on XRT event grades 0–4 (i.e., single and double pixel events) was applied to the data. Again, the spectrum was binned to ensure a minimum of 20 counts bin^{-1}. Energy channels below 0.3 keV and above 10.0 keV were excluded.

An absorbed power-law model fits the PC data well ($\chi_r^2 = 0.70$; 21 dof), with $N_H = 1.5^{+0.8}_{-0.7} \times 10^{21}$ cm^{-2} and $\beta = -1.10^{+0.27}_{-0.24}$.

No evidence is found for evolution of the X-ray spectral shape with time (cf. Chincarini et al. 2005).

2.3. *UVOT Data*

The *Swift* UVOT began taking data in the *V* filter ∼65 s after the burst trigger, immediately after the GRB came into its field of view. After about 10 s the spacecraft attitude had settled and UVOT began a 100 s "finding chart" exposure in *V*. Thereafter the instrument cycled through each of six color filters, *V*, *B*, and *U*, together with filters defining three ultraviolet passbands, UVW1, UVM2, and UVW2, with central wavelengths of 260, 220, and 193 nm, respectively. The exposure duration per filter was initially 10 s, subsequently increasing to 100 s and then to 900 s at predetermined times after the trigger. Data were taken in both "event mode," in which the time and detector position of each individual photon is recorded, and in "image mode," where the image is accumulated on board, discarding the photon timing information within an exposure to reduce telemetry volume. At some phases of the observation, both modes were operated

TABLE 3
UVOT Multicolor Data

$T(\text{mid})$[a] (s)	$T(\text{exp})$ (s)	Magnitude	Flux Density[b]
V Filter			
66	1.0	13.21 ± 0.24	189.8 ± 41.2
67	1.0	12.90 ± 0.23	254.0 ± 53.6
68	1.0	12.86 ± 0.23	263.3 ± 55.5
69	1.0	13.01 ± 0.23	227.9 ± 48.5
70	1.0	12.97 ± 0.23	236.3 ± 50.1
71	1.0	13.31 ± 0.23	172.8 ± 34.0
72	1.0	13.13 ± 0.23	204.3 ± 43.9
73	1.0	13.01 ± 0.23	227.9 ± 48.5
78	5.0	13.13 ± 0.10	204.3 ± 19.6
83	5.0	13.26 ± 0.10	181.5 ± 17.7
88	5.0	13.18 ± 0.10	195.5 ± 18.9
93	5.0	13.24 ± 0.11	185.6 ± 18.1
98	5.0	13.25 ± 0.11	184.2 ± 17.9
103	5.0	13.51 ± 0.11	144.9 ± 14.7
108	5.0	13.44 ± 0.11	154.4 ± 15.5
113	5.0	13.67 ± 0.11	124.7 ± 13.0
118	5.0	13.48 ± 0.11	148.4 ± 15.0
123	5.0	13.62 ± 0.11	130.2 ± 13.5
128	5.0	13.86 ± 0.12	104.2 ± 11.4
133	5.0	13.70 ± 0.11	121.5 ± 12.8
138	5.0	13.83 ± 0.12	107.2 ± 11.6
143	5.0	13.81 ± 0.12	109.2 ± 11.8
148	5.0	13.84 ± 0.12	106.2 ± 11.5
153	5.0	13.87 ± 0.12	103.2 ± 11.3
158	5.0	14.06 ± 0.12	87.1 ± 10.0
163	5.0	14.00 ± 0.12	91.7 ± 10.3
168	5.0	14.01 ± 0.12	90.8 ± 10.3
173	10.0	14.08 ± 0.13	83.3 ± 10.6
258	10.0	14.64 ± 0.14	49.8 ± 6.8
342	10.0	14.79 ± 0.15	43.3 ± 6.4
426	10.0	15.22 ± 0.17	29.2 ± 4.9
511	10.0	15.47 ± 0.19	23.2 ± 4.4
595	10.0	16.06 ± 0.24	13.4 ± 3.3
680	10.0	15.83 ± 0.22	16.6 ± 3.7
764	10.0	16.06 ± 0.25	13.4 ± 3.5
849	10.0	15.78 ± 0.22	17.4 ± 3.9
933	10.0	15.85 ± 0.24	16.3 ± 4.0
1243	100.0	16.34 ± 0.15	10.4 ± 1.5
18575	156.0	18.15 ± 0.41	2.0 ± 0.9
22163	580.0	19.10 ± 0.27	0.8 ± 0.2
35638	750.0	18.86 ± 0.27	1.0 ± 0.3
49320	4982.0	>20.62	<0.2
971360	33800.0	>22.09	<0.1
1171176	6081.0	>21.16	<0.1
B Filter			
229	10.0	14.79 ± 0.12	72.2 ± 8.4
313	10.0	15.19 ± 0.12	49.9 ± 5.8
397	10.0	15.51 ± 0.13	37.2 ± 4.7
482	10.0	15.63 ± 0.14	33.3 ± 4.6
571	10.0	15.70 ± 0.14	31.2 ± 4.3
651	10.0	16.13 ± 0.16	21.0 ± 3.3
735	10.0	16.03 ± 0.16	23.0 ± 3.7
820	10.0	16.56 ± 0.20	14.1 ± 2.9
904	10.0	16.44 ± 0.20	15.8 ± 3.2
1034	100.0	16.61 ± 0.11	13.5 ± 1.4
12671	390.0	18.59 ± 0.18	2.2 ± 0.4

TABLE 3—Continued

$T(\text{mid})$[a] (s)	$T(\text{exp})$ (s)	Magnitude	Flux Density[b]
16182	190.0	18.69 ± 0.17	2.0 ± 0.3
30031	388.0	19.82 ± 0.52	0.7 ± 0.4
33898	900.0	20.84 ± 0.45	0.3 ± 0.1
45468	896.0	>20.70	<0.3
62549	6513.0	>21.55	<0.1
U Filter			
215	10.0	13.70 ± 0.18	110.3 ± 19.9
299	10.0	14.08 ± 0.18	77.8 ± 14.0
419	10.0	14.47 ± 0.19	54.3 ± 10.4
468	10.0	14.71 ± 0.19	43.5 ± 8.3
552	10.0	14.97 ± 0.20	34.3 ± 6.9
637	10.0	15.01 ± 0.20	33.0 ± 6.7
721	10.0	15.14 ± 0.20	29.3 ± 5.9
805	10.0	15.46 ± 0.21	21.8 ± 4.7
890	10.0	15.29 ± 0.21	25.5 ± 5.4
975	10.0	15.32 ± 0.22	24.8 ± 5.6
12019	900.0	17.66 ± 0.17	2.9 ± 0.5
28664	194.0	18.85 ± 0.30	1.0 ± 0.3
29380	900.0	18.79 ± 0.20	1.0 ± 0.2
41040	758.0	19.99 ± 0.54	0.3 ± 0.2
52994	780.0	>19.68	<0.4
128928	1548.0	>20.05	<0.3
UVW1 (260 nm) Filter			
202	10.0	13.61 ± 0.07	162.8 ± 10.4
286	10.0	14.18 ± 0.09	96.3 ± 8.0
370	10.0	14.77 ± 0.12	56.2 ± 6.2
455	10.0	15.10 ± 0.14	41.5 ± 5.3
539	10.0	15.22 ± 0.15	37.0 ± 5.1
624	10.0	15.26 ± 0.15	35.6 ± 4.9
708	10.0	15.22 ± 0.15	36.9 ± 5.1
792	10.0	15.88 ± 0.21	20.1 ± 3.8
877	10.0	16.15 ± 0.24	15.7 ± 3.5
961	10.0	15.76 ± 0.20	22.6 ± 4.1
6761	638.0	17.33 ± 0.06	5.3 ± 0.3
28111	900.0	19.49 ± 0.19	0.7 ± 0.1
40585	900.0	20.33 ± 0.39	0.3 ± 0.1
52100	898.0	>21.05	<0.3
63738	900.0	>21.20	<0.3
UVM2 (220 nm) Filter			
187	10.0	13.54 ± 0.10	218.9 ± 20.0
272	10.0	14.32 ± 0.14	106.8 ± 14.1
356	10.0	14.60 ± 0.16	82.4 ± 12.4
440	10.0	14.94 ± 0.19	60.3 ± 10.7
525	10.0	15.84 ± 0.30	26.4 ± 7.2
609	10.0	14.90 ± 0.19	62.4 ± 10.8
694	10.0	15.18 ± 0.21	48.3 ± 9.4
778	10.0	15.51 ± 0.26	35.9 ± 8.5
863	10.0	15.57 ± 0.26	33.8 ± 8.1
947	10.0	15.66 ± 0.27	31.2 ± 7.6
5984	900.0	17.10 ± 0.06	8.2 ± 0.4
24007	864.0	18.96 ± 0.19	1.5 ± 0.3
39683	897.0	19.72 ± 0.30	0.7 ± 0.2
51257	900.0	20.34 ± 0.48	0.4 ± 0.2
74798	931.0	>21.59	<0.6

TABLE 3—*Continued*

T(mid)[a] (s)	T(exp) (s)	Magnitude	Flux Density[b]
UVW2 (198 nm) Filter			
245..................	10.0	14.69 ± 0.11	88.4 ± 9.5
329..................	10.0	15.30 ± 0.16	50.2 ± 7.2
413..................	10.0	15.13 ± 0.14	58.6 ± 7.7
498..................	10.0	15.60 ± 0.18	38.2 ± 6.4
582..................	10.0	15.22 ± 0.15	54.3 ± 7.5
666..................	10.0	15.80 ± 0.20	31.7 ± 5.8
751..................	10.0	15.72 ± 0.19	34.3 ± 5.9
835..................	10.0	16.43 ± 0.27	17.8 ± 4.5
920..................	10.0	16.21 ± 0.25	21.8 ± 4.9
1140................	100.0	16.35 ± 0.08	19.1 ± 1.5
17973..............	882.0	18.99 ± 0.13	1.7 ± 0.2
34806..............	900.0	20.05 ± 0.25	0.6 ± 0.1
52162..............	1800.0	>21.76	<0.3

[a] Time since trigger.
[b] Flux in units of 10^{-16} ergs cm^{-2} s^{-1} Å^{-1}.

simultaneously through differently sized spatial windows that were selected in combination with the spatial binning of the image-mode data so as to match the overall data volume with the available telemetry rate. The event mode and larger spatial windows are emphasized at the beginning of the observing sequence, when the afterglow brightness is changing rapidly and its position is less well known. Later in the sequence, only image-mode data are taken. The intrinsic spatial pixel size of the detector is approximately 0″.5 on the sky, but some image-mode data were taken with the data binned 2×2 to give 1″ pixels.

Examination of the UVOT finding chart exposure reveals a bright new fading source within the XRT positional error circle of the burst at R.A. = 18^{h}32^{m}32^{s}62, decl. = +26°20′21″6 (J2000.0) with an estimated uncertainty of 0″.2. This is close to the ROTSE (Robotic Optical Transient Search Experiment) position given by Rykoff et al. (2005).

In Figure 4 we show the light curves in each of the UVOT bands as a function of time. These data were derived from measurements made in a 6″ aperture, with background determined from a nearby source-free region. Since the UVOT detector counts individual photons, it is subject to coincidence loss (pileup), which is noticeable for count rates above 10 s^{-1}. We have applied the standard coincidence loss correction to the data, derived from ground calibrations (Breeveld et al. 2006). The data have also been corrected for Galactic extinction, adopting a value of $E(B - V) = 0.095$ for this field (Schlegel et al. 1998). We used the data of Schlegel et al. (1998) and Pei (1992) to derive extinction values for each filter. Expressed as magnitudes, these are 0.688 (UVW2), 0.926 (UVM2), 0.740 (UVW1), 0.518 (U), 0.412 (B), and 0.316 (V). The data are tabulated in Table 3, separated by filter. The detector count rates have been converted to magnitudes and fluxes on the basis of in-orbit calibration data. Systematic uncertainties between the filters are estimated to be better than 0.15 mag.

After the source had faded below the threshold of detectability through the UVOT color filters, we made observations in unfiltered (white) light. The white-light data provided detections of the afterglow beyond 10^5 s. We place the white-light data on the V magnitude and flux scale using a color-dependent correction that is derived by relating the measured ratio of V to white counts of field stars and photometric standards to their apparent $B - V$ color (i.e., $B - V$ color not corrected for reddening). The white-light data are given in Table 4.

TABLE 4
UVOT White Light

T(start) (s)	T(stop) (s)	Exposure	V Magnitude[a]	V Flux[b]
93,167..............	111,189	2378	21.35 ± 0.27	0.103 ± 0.025
173,859............	329,532	11750	22.82 ± 0.43	0.027 ± 0.010
329,532............	2,599,088	146267	>24.11	<0.008

[a] Equivalent V-band magnitude.
[b] Equivalent V-band flux, in units of 10^{-16} ergs cm^{-2} s^{-1} Å^{-1}.

2.3.1. Temporal Analysis

We fit a single power law to the light curve for each UVOT broadband filter individually, initially using only the data at $T \leq 1000$ s after the BAT trigger, where the sampling for each individual filter is relatively dense. Each filter can be reasonably fitted to a common slope of $\alpha = -1.14 \pm 0.01$. We conclude that there is no evidence for a gross change in the optical/UV spectrum associated with the temporal decay.

To maximize the light-curve sampling, we combine the data from all the UVOT filters, multiplying the individual curves by a factor that normalizes them to a common flux scale. The results are shown in Figure 5. We also include for comparison the X-ray decay curve of Figure 3, which has been multiplied by a constant factor in Figure 5 for display purposes. It can be seen that the X-ray and optical/UV signals initially fade at a similar rate, but that the optical/UV flux flattens compared to the X-ray curve in the interval 1000–10,000 s (i.e., the ratio of optical to X-ray flux increases with time). After about 10,000 s the optical curve steepens in a similar way to the X-ray curve.

The complex nature of the optical/UV light curve is confirmed by the fact that a single power law does not provide a good fit to the combined UVOT data over the entire time range. The χ^2 for the fit is 1038 for 115 degrees of freedom. We instead tried various combinations of power laws and found that the best fit was obtained when we fit three power-law components simultaneously. The model consists of the sum of two power laws (Holland et al. 2004) that breaks to a third, single power law at late time. This is physically consistent with the flux being dominated by a reverse shock at very early time, a forward shock at intermediate time, and a jet break at late time. The best-fitting model had an early-time power-law decay of $\alpha_1 = -1.56^{+0.07}_{-0.08}$ transitioning to a power law with a slope of $\alpha_2 = -0.62^{+0.05}_{-0.04}$ at $t_t = 432^{+173}_{-86}$ s. This transition time is the time at which both power-law components contribute equally to the observed flux from the afterglow. An achromatic break occurs at $t_j = 13,133^{+691}_{-691}$ s after the BAT trigger. We interpret this as a jet break. The decay index after the jet break is $\alpha_j = -1.76^{+0.08}_{-0.08}$. The time of the jet break, and the post-break index, are consistent with the values from the X-ray data. The χ^2 value for this model is 555 for 111 degrees of freedom, the high value reflecting significant short-term scatter of individual points about the model. This model is compared to the individual filter data in Figure 4.

Klotz et al. (2005) find that the R-band light curve of the GRB 050525a afterglow underwent a sudden rebrightening of 0.65 mag at 1968 s after the BAT trigger. This was at a time when GRB 050525a was not visible to *Swift*. We show the Klotz et al. data in Figure 6, normalized to the UVOT curve. If we add this rebrightening to our model, the best fit has $\alpha_1 = -2.14^{+0.25}_{-0.26}$, $\alpha_2 = -1.04^{+0.02}_{-0.02}$, $\alpha_j = -1.73^{+0.08}_{-0.11}$, $t_t = 39^{+6}_{-6}$ s, and $t_j = 17,747^{+1523}_{-1172}$ s, with a χ^2 value of 597 for 111 degrees of freedom. Although the χ^2 value is formally larger with a rebrightening,
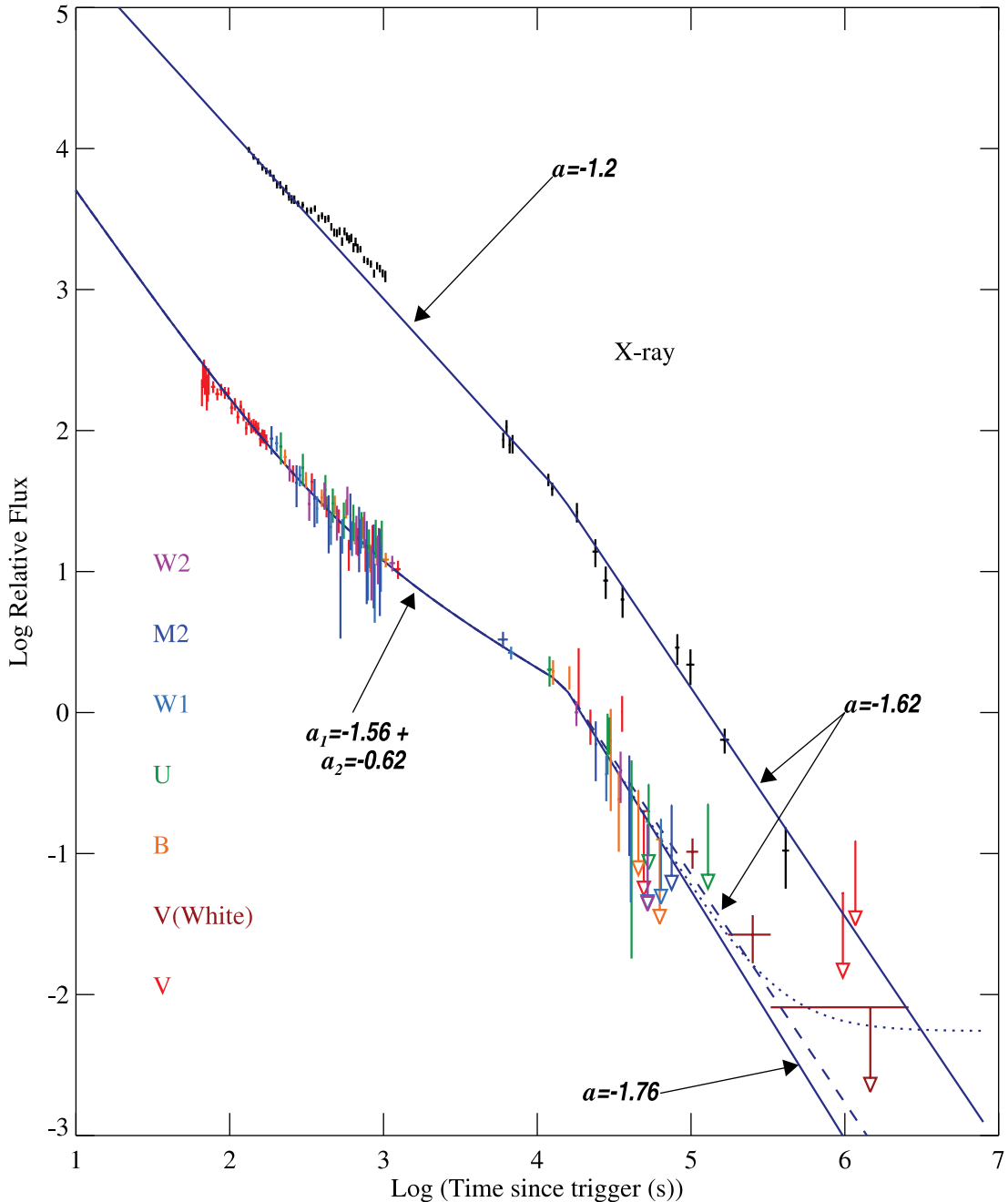
Fig. 5.—Comparison of flux decay in the X-ray and UVOT bands. The UVOT data have been normalized in the interval up to $T + 1000$ s, and the data taken through different filters are distinguished by color. The relative normalization of the X-ray and optical/UV data is arbitrary. The best-fit broken power-law model is plotted through the X-ray data. The best-fit double power law with break is plotted through the UVOT data (see text). The dashed line has the same postbreak slope as the X-ray data. The dotted line shows the best-fit model with a constant flux added, corresponding to the value measured by Soderberg (2005) using the *HST* ACS (see text).

an examination of Figures 4 and 6 suggests that both models provide comparable fits.

Soderberg (2005) has reported a late-time measurement of the GRB 050525a afterglow brightness using the *Hubble Space Telescope* (*HST*) Advanced Camera for Surveys (ACS). This is illustrated in Figure 6. The *HST* measurement is approximately 3 mag brighter than that predicted at this time by an extrapolation of our best-fit afterglow model. If the *HST* measurement represents a constant background flux, for example, due to the host galaxy or slowly varying supernova emission, then we estimate that this would contribute about 25% of the flux that we measure in our UVOT white-light detection at $\sim 2.5 \times 10^5$ s. The effect of

such a constant additional flux on the best-fit model is illustrated in Figure 5 by the dotted line.

2.3.2. *Multiwavelength Spectral Analysis*

Combining data across the *Swift* instruments provides a powerful set of diagnostics for prescribing the instantaneous spectral properties of a source and its temporal evolution. In order to fit an instantaneous spectral model to the UVOT data, it is necessary to interpolate count rates through each filter to a common epoch. We build a broadband spectrum of the source at $T + 250$ s, using the appropriate decay index for each filter and the nearest exposure to $T + 250$ s as a normalization reference. The XRT spectrum
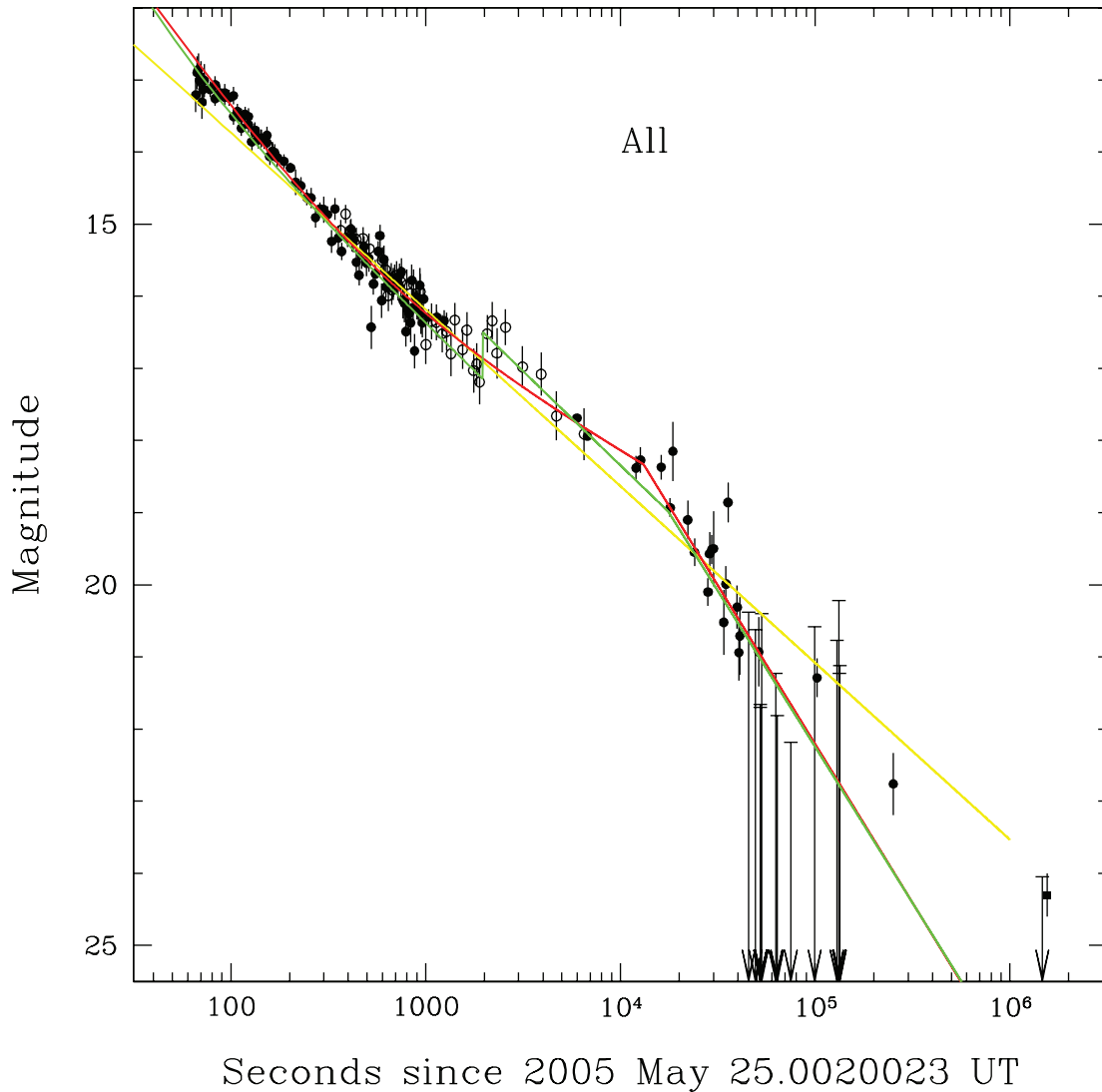
Fig. 6.—UVOT photometry (*filled circles*), normalized so that the early-time flux is the same in each filter. The red and green lines represent the models from Fig. 4. The yellow line shows the best-fitting single power law. The open circles show the Klotz et al. (2005) data, scaled to the same flux scale. The filled square shows the *HST* ACS F625W data of Soderberg (2005). Note that the *HST* ACS data point is approximately 3 mag brighter than the predicted afterglow magnitude.

described in § 2.2.2 was also renormalized to $T + 250$ s according to the early decay slope from Figure 3. As prior assumptions within the spectral model, we take the XRT slope and the 2–10 keV flux determined in § 2.2.2, the Galactic hydrogen column density in the direction of the source of 9×10^{20} cm^{-2} (Dickey & Lockman 1990), and the Galactic extinction in the same direction characterized by Pei (1992) with $E(B − V) = 0.095$ (Schlegel et al. 1998) and $R_V = 3.1$. Applying this model directly to the combined UVOT and XRT spectrum at $T + 250$ s yields a poor fit with $\chi^2 = 5.3 \times 10^4$ for 24 degrees of freedom. This particular model systematically overpredicts the optical and UV flux. We attempt to correct this by first adding dust extinction and gas absorption from the host galaxy at a fixed redshift of $z = 0.606$. The dust is initially assumed to have a content identical to the Small Magellanic Cloud (SMC) with $R_V = 2.93$ (Pei 1992). This does not provide an acceptable fit, with $\chi^2 = 272$ for 22 degrees of freedom, where N_H(host) $= (1.8 \pm 0.8) \times 10^{21}$ cm^{-2} and $E(B − V)$(host) $= 0.43 \pm 0.03$. Adopting host dust characteristics identical to the Galaxy and Large Magellanic Cloud (LMC) populations (Pei 1992) does not improve the fit significantly, yielding $\chi^2 = 208$ and 242, respectively for 22 degrees

TABLE 5
SED AT $T + 250$ s

Parameter	SMC	LMC	Galaxy
N_H(host) (cm^{-2})	$1.2 \pm 0.8 \times 10^{21}$	$1.2 \pm 0.8 \times 10^{21}$	$1.2 \pm 0.8 \times 10^{21}$
β_1	-0.60 ± 0.04	-0.63 ± 0.03	-0.62 ± 0.04
β_2[a]	-0.97	-0.97	-0.97
E_{break} (keV)	1.0 ± 0.2	1.0 ± 0.2	1.0 ± 0.2
$E(B − V)$(host)	0.04 ± 0.02	0.06 ± 0.03	0.06 ± 0.04
χ^2 (dof)	27 (20)	31 (20)	41 (20)

Notes.—Best-fit spectral parameters for the spectral energy distribution of GRB 050525a at $T + 250$ s for three dust populations assumed for the host galaxy. The model continuum is a broken power law (β_1 where $E < E_{break}$ and β_2 where $E > E_{break}$). The slope in the X-ray band, $\beta_2 = 0.97$, and the 2–10 keV flux are fixed at the values determined by XRT. Galactic values for gas absorption and dust extinction are used, while the gas and dust properties of the host galaxy [N_H(host) and $E(B − V)$(host)] are allowed to float.
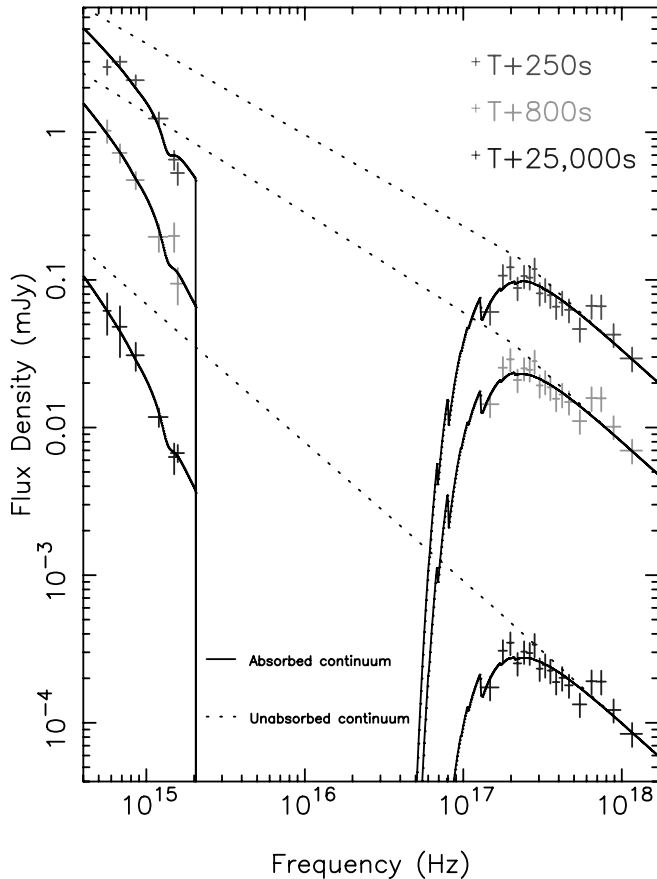
[a] Fixed parameter.

Fig. 7.—UVOT and XRT data, interpolated to the epochs $T + 250$ s, $T + 800$ s, and $T + 25,000$ s, and the best spectral fit models (*solid lines*). The dotted lines represent the intrinsic continuum of the source, before extinction and absorption from gas and dust in both the Milky Way and the host galaxy. [*See the electronic edition of the Journal for a color version of this figure.*]

TABLE 6
THE SMC-DUST MODEL FROM TABLE 5 APPLIED
TO THE GRB 050525a SED AT THREE EPOCHS

Parameter	$T + 250$ s	$T + 800$ s	$T + 25,000$ s
$N_{\rm H}$(host) (cm^{-2}).....	$1.2 \pm 0.8 \times 10^{21}$	$1.5 \pm 0.9 \times 10^{21}$	$1.8 \pm 1.0 \times 10^{21}$
β_1............................	-0.60 ± 0.04	-0.67 ± 0.06	-0.94 ± 0.10
β_2[a]	-0.97	-0.97	-0.97
$E_{\rm break}$ (keV)	1.0 ± 0.2	0.9 ± 0.2	...
$E(B - V)$(host)	0.04 ± 0.02	0.09 ± 0.04	0.08 ± 0.05
χ^2 (dof).................	27 (20)	18 (20)	15 (20)

[a] Fixed parameter.

spectra starting about 1 minute after the burst trigger and extending to several days after the burst, making this one of the best covered GRBs thus far. The ratio of the gamma-ray fluence to the X-ray flux is typical of the general population of long bursts observed in the pre-*Swift* era (cf. Roming et al. 2005).

In an initial period of about 4 hr after the burst, the decline of the X-ray afterglow flux of GRB 050525a can be well represented by a simple power law with an index of -1.2, apart from a probable flare that occurs after about 300 s. The optical temporal signature is more complex, however, and exhibits a significant flattening over that same period. It can be reproduced by the combination of two power laws (or two power laws combined with a rebrightening episode), one declining more rapidly than the X-ray flux, and the other more slowly. This can be interpreted as a steep reverse shock component, combined with the flatter optical apparition of the forward shock seen in X-rays. The X-ray and optical/UV multiwavelength spectral fits suggest that the cooling frequency of the electrons in the forward shock has moved through the optical band by 25,000 s after the burst. There is good evidence for a break in the time evolution of both the X-ray and optical/UV data at 13,000–14,000 s ($\sim$0.15 days) after the trigger. The break is consistent with being achromatic; i.e., the break time is, within the errors, consistent between the X-ray and optical bands, and the postbreak slope is also consistent within the errors (cf. §§ 2.2.1 and 2.3.1). Its achromatic nature suggests that this is the so-called jet break, which occurs when the beaming angle of the decelerating relativistic flow approaches the collimation angle of the jet (Sari et al. 1999).

If we compare the temporal and spectral indexes in both the UVOT band and the XRT band with the theoretical models (e.g., Table 1 in Zhang & Mészáros 2004), as well as the ordering of various temporal segments on the X-ray and optical light curves (Sari et al. 1998; Chevalier & Li 2000), we find that the global data are not consistent with a model that invokes a massive stellar wind. This is also supported by the fact that the spectral break energy $E_{\rm break}$ in our joint XRT-UVOT spectrum (which is consistent with a cooling break) evolves downward with time, since ν_c increases with time in the wind model. The UVOT-XRT data before $\sim$400 s could be accommodated with a slow-cooling wind model in which the UVOT band is between ν_m and ν_c [with the temporal index $(1 - 3p)/4$] while the X-ray band is above ν_c [with the temporal index $(2 - 3p)/4$]. However, the $\nu_m < \nu < \nu_c$ segment is expected to happen at a later time, and it is typically the last segment in the light curve, so it is very unlikely that there would be a switch back to a shallower decay in the wind model (Fig. 1 of Chevalier & Li 2000). The early steep-to-shallow transition observed in the UVOT light curve naturally rules out the wind interpretation and is consistent with a reverse-forward shock model as discussed below. Another possibility is that the fireball may be initially in a wind medium, but later runs into an interstellar medium (ISM)

of freedom. An acceptable fit is, however, obtained if we add a spectral break to the model at 1 keV. Details of the fits to the model with a spectral break are provided in Table 5. The table includes results obtained using SMC, LMC, and Galactic dust distributions. The SMC prescription is preferred statistically over the other two.

We then perform spectral fits using the broken power-law model with SMC-like dust in the host galaxy for two other epochs, $T + 800$ s and $T + 25,000$ s. Data and best-fit models are plotted in Figure 7, while best-fit parameters are listed in Table 6. Other than temporal decay, we find no evidence for spectral evolution between 200 and 800 s after the burst; the spectral break has not moved within errors. However, at $T + 25,000$ s the spectrum no longer requires a break between the XRT and UVOT energy bands. The UVOT spectral index is identical to the XRT index, within the measurement uncertainties. There is no evidence for evolution in the host's gas or dust environments over these epochs.

3. DISCUSSION

GRB 050525a is the second most fluent GRB to have been observed by *Swift* to date and is the first bright low-redshift burst to have been observed since all three *Swift* instruments have been operational. The hard X-ray/gamma-ray temporal characteristics and spectrum of this bright burst have been well characterized by the BAT. In addition, the XRT and UVOT instruments provide well-sampled temporal multiwavelength decay light curves and

after it crosses a wind-termination shock. An additional motivation for this interpretation is the optical rebrightening at ~ 2000 s revealed by the TAROT data (Télescope à Action Rapide pour les Objets Transitoires; Klotz et al. 2005), which could be presumably the signature of the termination shock. Although the possibility that the rebrightening is due to a density enhancement in the medium surrounding the burst is promising, the above scenario lacks direct proof, since the wind signature, if it is one, terminates at a much earlier time (e.g., ~ 400 s) than the epoch of the optical rebrightening bump.

Instead, the XRT and UVOT data before the presumed jet break at 0.15 days are in good agreement with the standard fireball model for a constant ISM density (e.g., Sari et al. 1998). According to this model, the spectral indexes (β) above and below the synchrotron cooling frequency ν_c are $-p/2$ and $-(p-1)/2$, respectively, while the temporal indexes (α) for a band that is above and below ν_c are $(3-3p)/4$ and $(2-3p)/4$, respectively. If we interpret E_{break} as the cooling break and take $p = 2.2$, one expects $\alpha_X = -1.15$, $\alpha_O = -0.9$, $\beta_X = -1.1$, and $\beta_O = -0.6$. All these are in general agreement with the data, particularly when the optical rebrightening at ~ 2000 s (Klotz et al. 2005) is taken into consideration when fitting model parameters. At $T + 25,000$ s, the energy spectrum of the burst is consistent with a single power-law spectrum extending between the XRT and UVOT bands, with index $\beta \sim -0.95$. This is consistent with the fact that the cooling frequency has already crossed the UVOT band at this epoch. The expected decay slope in the UVOT band should be approximately -1.15 in the standard model. The observed decay slope at this time, however, is steeper (approximately -1.6). This is due to the existence of a jet break around $\sim T + 14,000$ s. According to the standard afterglow model, ν_c evolves with time as $\propto t^{-1/2}$. The data, on the other hand, requires a slightly faster evolution of E_{break}. Enhanced cooling is thus needed, possibly with an evolving ϵ_B, the magnetic equipartition parameter in the shock. An evolving ϵ_B was also invoked to interpret data for GRB 050128 (Campana et al. 2005).

A temporal break is identified in the X-ray light curve at around 14,000 s (0.15 days). The UVOT data show a break around the same time. Since there is no apparent spectral change across the break, and since the break time is "achromatic," this points to a jet break, corresponding to the time when the fireball Lorentz factor $\gamma \sim 1/\theta_j$ (Rhoads 1999; Sari et al. 1999). The postbreak temporal index, however, is shallow (approximately -1.6) compared with the model prediction (which is approximately $-p = -2.2$). Such a shallow jet break has also been seen previously in some other bursts (e.g., GRB 990123; Kulkarni et al. 1999). It might be shallow because the sideways expansion effect is not significant (Panaitescu & Mészáros 1999). Another possibility is that the jet break turnover time may be finite (Panaitescu & Mészáros 1999), so that the postbreak asymptotic regime has not yet been reached. If this is the case, then the effective jet break time could be later than we have fitted. For example, while the increased number of free parameters are not justified by the quality of our data, we could force a fit with three power laws to our X-ray data with a second break to a slope of $\alpha = -2.2$ at about $T = 1-1.5 \times 10^5$ s, yielding an "effective" single break time of about 50,000–60,000 s. This is illustrated in Figure 3, where the dash-dotted line shows a break to a slope of $\alpha = -2.2$ at $T = 1.5 \times 10^5$ s. The final two XRT points in isolation are equally consistent with slopes of $\alpha = -1.6$ and -2.2. It is also still possible that the observed temporal break is due to reasons other than a jet break (e.g., Gendre & Boër 2005), but given that this is the first time one sees an achromatic break in both the X-ray and

the optical band, we tentatively conclude that the current data support a jet break interpretation.

If the break is indeed attributed to a jet, one can derive a jet angle (e.g., Sari et al. 1999)

$$
\begin{aligned}
\theta_j &= 0.12 \left(\frac{t_j}{1+z} \right)^{3/8} \left(\frac{n_0 \eta_\gamma}{E_{\mathrm{iso,\,53}}} \right)^{1/8} \\
&= (5.6 \times 10^{-2}) \left(\frac{n_0 \eta_\gamma}{0.6} \right)^{1/8} \left(\frac{t_j}{0.15 \text{ days}} \right)^{3/8},
\end{aligned} \tag{1}
$$

where t_j is expressed in units of days, n_0 is the ambient density, η_γ is the ejecta-to-gamma-ray efficiency, and $E_{\mathrm{iso,\,53}}$ is the isotropic energy in units of 10^{53} ergs. In our calculations we use $n_0 = 3$ cm^{-3} and $\eta_\gamma = 0.2$ (Ghirlanda et al. 2004). Therefore, $\theta_j \sim 3°.2$ if we use a jet break time of $t_j \sim 0.15$ days, or $\theta_j \sim 5°.4$ if we adopt a more conservative jet break time of $t_j \sim 0.6$ days, corresponding to a finite roll-over as discussed above; these two values bracket the possible range of values of t_j. This angle could be interpreted as the physical opening angle of a jet if the jet has a uniform distribution of energy or as the observer's viewing angle with respect to the jet axis in a structured jet model (Rossi et al. 2002; Zhang & Mészáros 2002; Kumar & Granot 2003). Within the uniform jet model, we estimate the actual gamma-ray energy emitted to be $E_\gamma = E_{\mathrm{iso},\gamma}(1 - \cos \theta_j) = 3.6 \times 10^{49}$ ergs for $t_j \sim 0.15$ days or $E_\gamma = 1.0 \times 10^{50}$ ergs for $t_j \sim 0.6$ days.

We can combine the information on the jet with the measurements of the redshift, E_p, $E_{\mathrm{iso},\gamma}$, t_j, and the lag between the high-energy and low-energy gamma-ray light curves (§ 2.1) to test whether this burst is consistent with various proposed empirical relations. Four relations involve E_{pt}, the peak energy in the burst frame for the entire burst: the Amati relation, $E_{\mathrm{pt,\,A}} \propto E_{\mathrm{iso}}^{0.5}$ (Amati et al. 2002), the Ghirlanda relation, $E_{\mathrm{pt,\,G}} \propto E_\gamma^{0.7}$ (Ghirlanda et al. 2004), the Yonetoku relation, $E_{\mathrm{pt,\,Y}} \propto L_{\mathrm{iso}}^{0.5}$ (Yonetoku et al. 2004), and the Liang-Zhang relation, $E_{\mathrm{pt,\,LZ}} \propto E_{\mathrm{iso}}^{0.52} t_j^{0.64}$ (Liang & Zhang 2005). For the values of E_{iso}, E_γ, t_j, and L_{iso} for GRB 050525a, we calculate $E_{\mathrm{pt,\,A}} = 144$ keV, $E_{\mathrm{pt,\,G}} = 46$ keV (if $t_j = 0.15$ days; 96 keV if $t_j = 0.6$ days), $E_{\mathrm{pt,\,Y}} = 186$ keV, and $E_{\mathrm{pt,\,LZ}} = 50$ keV (if $t_j = 0.15$ days; 122 keV if $t_j = 0.6$ days), which should be compared to the observed value of $E_{\mathrm{pt}} = 126.6 \pm 5.5$ keV. The set of bursts used to calibrate these relations is small enough that each additional burst with a redshift and a spectrum changes the relations quantitatively; in addition, there is significant scatter around these relations (G. Ghirlanda 2005, private communication).

According to the lag-luminosity relation, shorter lags between the emission in two gamma-ray bands are correlated with larger values of L_{iso} (Norris et al. 2000). Using the methodology in Band et al. (2004), we calculate a redshift $\hat{z} = 0.69 \pm 0.02$ for GRB 050525a from the observed values of the peak flux, lag, and spectrum at the peak of the light curve (Norris et al. 2005); the uncertainty in this derived time-lag redshift accounts for the uncertainty in the lag and the peak flux, but not for the systematic uncertainty resulting from the somewhat different energy bands used to calibrate the lag-luminosity relation and for the Swift observation. Given the large redshift range over which bursts are detected, the agreement between this time-lag redshift and the spectroscopic redshift is impressive.

The UVOT light curves are consistent with the existence of an early reverse shock component (Mészáros & Rees 1997; Sari & Piran 1999). The best-fit initial decay index is sensitive to whether we include a rebrightening episode in our model, as suggested by Klotz et al. (2005). It ranges from $\alpha_1 \sim -1.5$ without rebrightening to $\alpha_1 \sim -2.1$ with rebrightening. This is in the range

observed for previous suggested detections of the reverse shock in GRB 990123 (Akerlof et al. 1999) and GRB 021211 (Fox et al. 2003; Li et al. 2003), which are typically approximately -1.9. A shallower decay corresponds to a shallower electron index in the reverse shock region, $p = (-4\alpha_1 - 1)/3 \sim 1.75$ (Zhang et al. 2003). In contrast with Shao & Dai (2005), who interpreted the tentative jet break as the forward shock peak, in our best fit, the forward shock peaks at a much earlier time, before 400 s. This corresponds to a typical "flattening"-type early afterglow (Zhang et al. 2003), which usually requires a magnetized central engine (see also Fan et al. 2002; Kumar & Panaitescu 2003). The best-fit

temporal index that we derive for the forward shock component in the optical/UV without a rebrightening is -0.62, flatter than the expectation of the simplest model (-0.9). However, if we include a rebrightening episode as described above, the slope of the forward shock component steepens to -1.04, which would be more consistent with the simple model.

REFERENCES

Akerlof, C., et al. 1999, Nature, 398, 400
Amati, L., et al. 2002, A&A, 390, 81
Arnaud, K. A. 1996, in ASP Conf. Ser. 101, Astronomical Data Analysis Software and Systems V, ed. G. H. Jacoby & J. Barnes (San Francisco: ASP), 17
Band, D., et al. 1993, ApJ, 413, 281
———. 2005, GCN Circ. 3466, http://gcn.gsfc.nasa.gov/gcn/gcn3/3466.gcn3
Band, D. L., Norris, J. P., & Bonnell, J. T. 2004, ApJ, 613, 484
Barthelmy, S., et al. 2006, Space Sci. Rev., in press
Breeveld, A. A., et al. 2006, SPIE, in press
Burrows, D. N., et al. 2005, Science, 309, 1833
———. 2006, Space Sci. Rev., in press
Campana, S., et al. 2005, ApJ, 625, L23
Chevalier, R. A., & Li, Z.-Y. 2000, ApJ, 536, 195
Chincarini, G., et al. 2005, ApJ, submitted (astro-ph/0506453)
Cummings, J., et al. 2005, GCN Circ. 3479, http://gcn.gsfc.nasa.gov/gcn/gcn3/3479.gcn3
Dickey, J. M., & Lockman, F. J. 1990, ARA&A, 28, 215
Fan, Y.-Z., Dai, Z.-G., Huang, Y.-F., & Lu, T. 2002, Chinese J. Astron. Astrophys., 2, 449
Foley, R. J., Chen, H.-W., Bloom, J., & Prochaska, J. X. 2005, GCN Circ. 3483, http://gcn.gsfc.nasa.gov/gcn/gcn3/3483.gcn3
Fox, D. W., et al. 2003, ApJ, 586, L5
Gehrels, N., et al. 2004, ApJ, 611, 1005
Gendre, B., & Boër, M. 2005, A&A, 430, 465
Ghirlanda, G., Ghisellini, G., & Lazzati, D. 2004, ApJ, 616, 331
Golenetskii, S., et al. 2005, GCN Circ. 3474, http://gcn.gsfc.nasa.gov/gcn/gcn3/3343.gcn3
Gotz, D., Mereghetti, S., Mowlavi, N., Shaw, S., Beck, M., Borkowski, J., & Lund, N. 2005, GCN Circ. 3472, http://gcn.gsfc.nasa.gov/gcn/gcn3/3472.gcn3
Holland, S. T., et al. 2004, AJ, 128, 1955
Klotz, A., Boër, M., Atteia, J. L., Stratta, G., Behrend, R., Malacrino, F., & Damerdji, Y. 2005, A&A, 439, L35

Kulkarni, S. R., et al. 1999, Nature, 398, 389
Kumar, P., & Granot, J. 2003, ApJ, 591, 1075
Kumar, P., & Panaitescu, A. 2003, MNRAS, 346, 905
Li, W., Filippenko, A. V., Chornock, R., & Jha, S. 2003, ApJ, 586, L9
Liang, E., & Zhang, B. 2005, ApJ, 633, 611
Mereghetti, S., et al. 2005, GCN Circ. 3477, http://gcn.gsfc.nasa.gov/gcn/gcn3/3477.gcn3
Mészáros, P., & Rees, M. J. 1997, ApJ, 476, 232
Norris, J., et al. 2005, GCN Circ. 3484, http://gcn.gsfc.nasa.gov/gcn/gcn3/3484.gcn3
Norris, J. P., Marani, G. F., & Bonnell, J. T. 2000, ApJ, 534, 248
Panaitescu, A., & Mészáros, P. 1999, ApJ, 526, 707
Pei, Y. 1992, ApJ, 395, 130
Piro, L., et al. 2005, ApJ, 623, 314
Rhoads, J. E. 1999, ApJ, 525, 737
Roming, P., et al. 2006a, Space Sci. Rev., in press
———. 2006b, ApJ, submitted (astro-ph/0509273)
Rossi, E., Lazzati, D., & Rees, M. J. 2002, MNRAS, 332, 945
Rykoff, E. S., Yost, S. A., Swan, H., & Quimby, R. 2005, GCN Circ. 3468, http://gcn.gsfc.nasa.gov/gcn/gcn3/3468.gcn3
Sari, R., & Piran, T. 1999, ApJ, 517, L109
Sari, R., Piran, T., & Halpern, J. P. 1999, ApJ, 519, L17
Sari, R., Piran, T., & Narayan, R. 1998, ApJ, 497, L17
Schlegel, D. J., Finkbeiner, D. P., & Davis, M. 1998, ApJ, 500, 525
Shao, L., & Dai, Z. G. 2005, ApJ, 633, 1027
Soderberg, A. 2005, GCN Circ. 3550, http://gcn.gsfc.nasa.gov/gcn/gcn3/3550.gcn3
Yonetoku, D., Murakami, T., Nakamura, T., Yamazaki, R., Inoue, A. K., & Ioka, K. 2004, ApJ, 609, 935
Zhang, B., Kobayashi, S., & Mészáros, P. 2003, ApJ, 595, 950
Zhang, B., & Mészáros, P. 2002, ApJ, 571, 876
———. 2004, Int. J. Mod. Phys. A, 19, 2385